Polymer 54 (2013) 6242–6252

Contents lists available at ScienceDirect

Polymer

journal homepage: www.elsevier.com/locate/polymer

Formation of mesomorphic domains associated with dimer aggregates of phenyl rings in cold crystallization of poly(trimethylene terephthalate)

Jian-Bang Jheng [a], Wei-Tsung Chuang [b, *], Po-Da Hong [a, *], Yen-Chih Huang [b], U-Ser Jeng [b], Chun-Jen Su [b], Guan-Rong Pan [c]

[a] Department of Materials Science and Engineering, National Taiwan University of Science and Technology, Taipei 10607, Taiwan, ROC
[b] National Synchrotron Radiation Research Center, Hsinchu 30076, Taiwan, ROC
[c] Biomaterials Section, Department of Raw Materials and Yarns, Taiwan Textile Research Institute, New Taipei City 23674, Taiwan, ROC

ARTICLE INFO

Article history:
Received 14 May 2013
Received in revised form
6 August 2013
Accepted 7 September 2013
Available online 17 September 2013

Keywords:
Cold crystallization
Mesomorphic domains
Poly(trimethylene terephthalate)

ABSTRACT

During the cold crystallization of poly(trimethylene terephthalate), PTT, multistage preordering activities associated with hierarchically structural evolution and origin of mesomorphic domains were investigated with time-resolved Fourier transform infrared (FTIR), photoluminescence (PL) and dielectric spectra (DS), and simultaneous small- and wide-angle X-ray scattering (SAXS/WAXS). The observed fluorescent emission at 390 nm and an absorption band at 874 cm^{-1} associated with the CH out-of-plane bending mode of the phenyl rings indicate that the ground-state dimers resulting from the phenyl rings of PTT chains via π–π interactions are formed in supercooled amorphous liquids. The time dependences of the increase of the fluorescent intensities, the wavenumber shift from 874 to 872 cm^{-1}, the conformational transformation of the trimethylene glycol units from *trans* to *gauche*, the dynamic α-to-α′ transition of the dielectric loss and the structural parameters reveal that the dimer aggregation accompanying a locally nematic-like orientation induced large phase-separated mesomorphic domains (over several tens of nanometers); nucleations of nanograin type (over several nm) subsequently formed within the mesomorphic domains after the conformational transformation form *trans* to *gauche* for the cold crystallization at 50 °C. Herein, we propose a preordering mechanism of cold crystallization in which the π–π interactions among the dimers serve as ordering bonding forces to drive intermolecular cooperativity before intramolecular changes of conformation, and the dimer aggregation triggers the phase-separated mesomorphic domains before the growth of crystalline nanograins (non-lamellar crystals). As distinct from the hierarchical structure of nanograins within mesomorphic domains, the formation of lamellar crystallites within spherulites without undergoing the dimer aggregation were observed form the melt crystallization at 200 °C.

Crown Copyright © 2013 Published by Elsevier Ltd. All rights reserved.

1. Introduction

The crystallization of a polymer involves sequential and cooperative chain activities, such as disentanglement, diffusion, absorption and conformational changes, among inter- and intramolecular assemblies [1–6]. These chain activities before three-dimensional (3D) chain packing (crystallization), a so-called '*preordering*', are an important aspect of understanding the relation between structural formation and physical properties. Several authors have considered mesomorphic (or intermediate) phases [7–15] or liquid–liquid phase separation [16–21] (via mechanism of nucleation and growth or spinodal decomposition) during the preordering. Such a formation of mesomorphic structures during the preordering is associated with a more-or-less ordered packing of parallel chains with significantly favored conformations and enhanced density in zones of semi-ordered arrangements. These mesomorphic structures have commonly been observed when crystallization occurs in deep supercooling or near glass transitions. Various interpretative models or mechanisms for the mesomorphic structures (e.g., paracrystalline [7,8], nodular [9], bundle [10,11], nanograin [13–15] and spinodal-like [16–20]) have hence been proposed for various polymers.

* Corresponding authors.
E-mail addresses: weitsung@nsrrc.org.tw (W.-T. Chuang), poda@mail.ntust.edu.tw (P.-D. Hong).

0032-3861/$ – see front matter Crown Copyright © 2013 Published by Elsevier Ltd. All rights reserved.
http://dx.doi.org/10.1016/j.polymer.2013.09.006

In our preceding work [22], we investigated the isothermal cold crystallization of poly(trimethylene terephthalate) (PTT) using simultaneous small- and wide-angle X-ray scattering and differential scanning calorimetry (SAXS/WAXS/DSC) and transmission electron microscope (TEM). An atypical hierarchical structure of nanograins within mesomorphic domains was firstly evidenced by TEM. Moreover, from SAXS/WASX/DSC results we observed that the growth of phase-separated mesomorphic domains (size ca. 50 nm) featuring unusual small-angle scattering emerged; an accompanying formation of nanocrystalline grains (of several nanometer-scale) then evolved within the mesomorphic domains. The formation of the mesomorphic domains indicated the transient coexistence of liquids in two forms in the induction stage of cold crystallization of PTT, as a liquid–liquid phase separation, whereas the physical origin and structural characters of the large-scale mesomorphic domains remained elusive, even though we investigated the crystallization behavior of PTT [22–28], and Jeng and coworkers clarified the mechanism of nanograin growth during the cold crystallization of poly(9,9-di-*n*-octyl-2,7-fluorene) [13],syndiotactic poly(styrene) [14] and poly(9,9-di-n-hexyl-2,7-fluorene) [15]on the basis of simultaneous SAXS/WAXS/DSC.

Somewhat similar to our observation of the unusual small-angle scattering in the cold crystallization of PTT (devitrification), but in vitrification of noncystalline polymers, Debye and Bueche [29] found an unusual small-angle scattering associated with the existence of long-range fluctuations of correlation length ca. 200 nm. Strong unusual small-angle scattering due to large-scale fluctuations, the so-called Fischer clusters, were observed near the glass-transition temperature in supercooled liquids of small molecules and polymers [30,31].Even if these results reveal that the vitrification of deeply supercooled liquids might induce these large-scale fluctuations, the structural nature of Fischer clusters remains unclear.

In the present work, we endeavored to investigate the origin of mesomorphic domains formed in the induction stage of cold crystallization of PTT using time-resolved measurements of SAXS/WAXS, Fourier-transform infrared (FTIR), photoluminescence (PL), and dielectric spectra (DS). PL and infrared spectra provide powerful and effective tools to examine in real time the variation of microstructures and chain conformation during crystallization. Having in their main chains fluorescent phenylene units that act as chromophores, the terephthalic-acid polyesters of PTT emit fluorescence that might be assigned to a ground-state dimer or excimer in the amorphous region [32,33]. The ground-state dimer resulting from interactions between main-chain phenyl rings generally exists stably in the ground state whereas the excimer exists in the excited state. We demonstrated that the supercooled liquid of a quenched PTT sample lacks a homogeneous random structure, but phenyl–phenyl dimers exist via π–π interactions. From an integration of time-resolved data, we propose that dimer aggregation via π–π interactions induces phase-separated mesomorphic domains during the induction stage of cold crystallization of PTT; this aggregation yields morphologies varied from the typical crystalline lamellae in the melt crystallization at high temperatures.

2. Experiments

Sample. Poly(trimethylene terephthalate) (PTT) (glass-transition temperature $T_g \approx 45$ °C and equilibrium melting temperature $T_m^0 \approx 242$ °C) [23] pellets of specific gravity 1.34 and intrinsic viscosity 0.92 dL/g (60/40 phenol/tetrachloroethane, 160 °C), were supplied by Shell Chemical. Glassy amorphous samples were prepared through melt-pressing at 260 °C for 5 min followed by quenching into iced water. Three sample thicknesses, 500, 60 and 30 μm, were used for SAXS/WAXS, dielectric and other spectral measurements, respectively.

Measurements. Fluorescence emission spectra were collected with a fluorescence spectrometer (FLS920) at interval 25 s during the isothermal crystallization. An amorphous PTT film was set at 45° to the exciting beam; the excitation wavelength was set to 322 nm [32], with spectral slit of 5 nm widths for both excitation and emission monochromators. Time-resolved FTIR spectra were measured (Nicolet 8700 Research FTIR spectrometer, Thermo Fisher Scientific Inc., equipped with a Hg–Cd–Te detector). The amorphous PTT film was isothermally measured (Linkam TST350 stage). FTIR spectra were recorded at resolution 1 cm^{-1} and interval 15 s during isothermal crystallization. SAXS/WAXS were performed in situ at SWAXS beamline 23A of National Synchrotron Radiation Research Center (NSRRC), Taiwan [34]. The amorphous PTT film was placed on a heating stage (Mettler Toledo FP84) and isothermally crystallized at 50 °C for measurement. With the incident beam ($\lambda = 1.550$ Å) offset from the center of the area detector (MAR165-CCD) for a wider SAXS q-range, the optimized geometry of the SAXS/WAXS setup covered the main WAXS and SAXS signals of PTT crystals in the q-ranges5 ~ 25 nm^{-1} and 0.05–1.5 nm^{-1}, respectively [35]. Dielectric loss was measured over frequency range 10^{-1}–10^4 Hz with an impedance analyzer (Solartron 1260) with a dielectric interface (Solartron 1296) for highly resistive samples. The amorphous PTT film was placed between parallel gold-plated electrodes of diameter 20 mm. Isothermal dielectric loss was measured at interval 60 s on a hot stage (Linkam TST350 stage). Notably, all the hot stages were calibrated in temperature by using standard samples of indium and zinc in order to make sure equivalent rate of isothermal crystallization for the different experimental methods.

Data Analysis. In the cold crystallization, the SAXS intensity profiles observed as a function of time in the low-q range (0.05–0.3 nm^{-1}) were modeled with the Guinier approximation [36]:

$$I(q,t) = I_0 \exp\left(-q^2 R_g^2/3\right) \tag{1}$$

for radius R_g of gyration of the scattering particles (corresponding to the large mesomorphic domains in this work). Here, $I_0 = n_p(\Delta\rho V)^2$ is a prefactor depending on the concentration n_p of scattering particles, particle volume V, and scattering contrast $\Delta\rho$. SAXS intensity profiles in the region of intermediate to large q (0.4–1.5 nm^{-1}) contributed mainly by small PTT crystallites were modeled with $I(q,t) = n_p P(q,t) S(q,t)$, using disk form factor $P(q,t)$ and a hard-sphere structure factor $S(q,t)$. For disks of thickness L and radius R, averaged over random spatial orientations [36]:

$$P(q,t) = 16\left(\pi R^2 L\right)^2 \Delta\rho^2 \int_0^1 \left[\frac{J_1\left(qR\sqrt{1-x^2}\right)\sin(qLx/2)}{q^2 R\sqrt{1-x^2}Lx}\right]^2 dx \tag{2}$$

where J_1 is a Bessel function of first order. In the Percus-Yevick (PY) expression [37–39], the structure factor of hard spheres,

$$S(q,t) = 1/[1 + 24\phi G(A)/A]] \tag{3}$$

is defined by the volume fraction φ and the effective hard-sphere diameter d, with $A = qd$ and

$$G(A) = \frac{\alpha}{A^2}(\sin A - A\cos A) + \frac{\beta}{A^3}\left[2A\sin A + \left(2 - A^2\right)\cos A - 2\right] + \frac{\gamma}{A^5}\left\{-A^4\cos A + 4\left[\left(3A^2 - 6\right)\cos A + \left(A^3 - 6A\right)\sin A + 6\right]\right\} \tag{4}$$

where $\alpha = (1+2\varphi)^2/(1-\varphi)^4$, $\beta = -6\varphi\,(1+\varphi/2)^2/(1-\varphi)^4$, and $\gamma = 0.5\varphi\,(1+2\varphi)^2/(1-\varphi)^4$. The mean spacing ξ of the particles is deduced from n_p determined by the volume fraction and the size of hard sphere [13].

In the melt crystallization of PTT, the crystalline-amorphous structure is typically analyzed in terms of a one-dimensional stack model, in which the stacks consist of crystalline lamellae separated by amorphous layers, using the one-dimensional correlation function $\gamma(x)$, defined as follows [40]:

$$\gamma(x,t) = \frac{1}{Q}\int_0^\infty I(q,t)q^2\cos(qx)\mathrm{d}q \tag{5}$$

where $I(q)$ is the scattered intensity; scattering invariant Q is expressed as

$$Q = \int_0^\infty I(q,t)q^2\mathrm{d}q \tag{6}$$

$\gamma(x)$ is normalized by $Q\,(\gamma(0)=1)$. As SAXS data are collected in a limited angular range, they must be extrapolated to both large q and small q. The extension to large q is performed with a Porod–Ruland model [41], according to which $I(q)$ is described with $I(q,t) = K_p(\exp(-\sigma^2q^2)/q^4) + I_b$, in which K_p is the Porod constant, I_b is the background intensity arising from the thermal fluctuation of density, and σ is related to the thickness of the crystalline-amorphous interface. The extrapolation to zero q data is obtained on fitting the intensity curve in the range of small q with the Debye-Bueche model [42,43], $I(q,t) = I(0,t)/(1+q^2\zeta^2)^2$, in which ζ is the correlation length.

Two-dimensional infrared correlation spectra (2D-IR) and time-resolved WAXS profiles (2D-WAXS) were recorded with software (2D Shige, composed by Shigeaki Morita, Kwansei Gakuin University, Sanda, Hyogo, Japan) [44,45]. Twenty spectra with an equal time interval in the wavenumber range 960–800 cm^{-1} for 0–3000 s and in the q-region 9–21 nm^{-1} for 0–1200 s were respectively selected for the 2D-IR and the 2D-WAXS correlation analyses. The time-averaged reference spectra were shown at the side and top of the 2D correlation maps for reference. In the synchronous 2D-IR and 2D-WAXS correlation spectrum, the auto peaks are located along the diagonal; the cross peaks are positioned at off-diagonal positions for the synchronous and asynchronous 2D-correlation spectra. In the 2D-correlation spectrum, a red-shaded area and a blue-shaded area represent regions of positive and negative intensity, respectively.

Dielectric loss data are described in terms of Havriliak–Negami equation [46]. This empirical equation shows the imaginary part of the dielectric constant as follows,

$$\varepsilon^* = \varepsilon_\infty + \sum_{j=\alpha,\alpha'}\frac{\Delta\varepsilon_j}{\left[1+(i\omega t_j)^{b_j}\right]^{c_j}} + \left(\frac{\sigma}{\omega}\right)^s \tag{7}$$

where ω is the angular frequency ($\omega = 2\pi F$, with circular frequency F), $\Delta\varepsilon$ is the dielectric strength of the relaxation of process j, b_j and c_j are shape parameters defined with the Havriliak–Negami equation, t_j is the most probable value of the distribution of relaxation time, and σ and s are parameters determining the contributions from the dc electric conductivity. The average relaxation time τ_j was calculated with this equation [47],

$$\tau_j = \frac{1}{2\pi F_{max}} = t_j\left[\sin\frac{b_j\pi}{2+2c_j}\right]^{-1/b_j}\left[\sin\frac{b_jc_j\pi}{2+2c_j}\right]^{1/b_j} \tag{8}$$

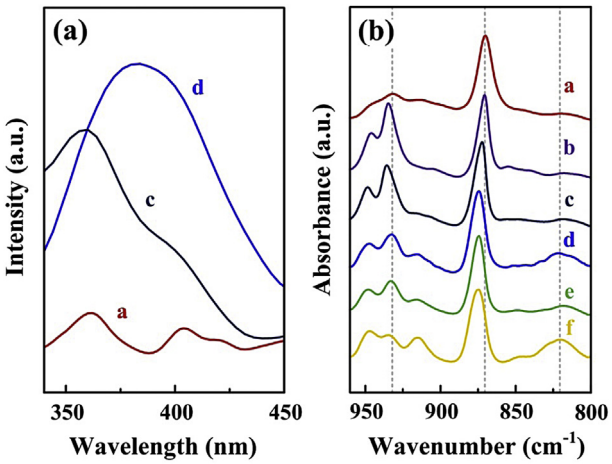

Fig. 1. (a) Fluorescence spectra (excitation $\lambda_{ex} = 322$ nm) and (b) FTIR spectra of PTT; a, molten state; b, melt-crystallized film at 170 °C; c, cold-crystallized film at 50 °C; d, quenched amorphous film; e, quenched amorphous film after aging at 30 °C for 24 days; f, quenched amorphous film after being cold drawn at draw ratio 2 and 30 °C.

3. Results

Identification of dimer characters of PTT by PL and FTIR spectra. Fig. 1a shows three fluorescence spectra for various PTT films. In the quenched amorphous film, a broad fluorescent peak emerged about 385 nm, in contrast to a peak at 360 nm observed from two other films in crystalline and molten states. Having in main chains fluorescent phenylene units, which act as chromophores, terephthalic acid polyesters typically emit fluorescence in a range 360–390 nm, which is attributed to a ground-state dimer or to an excimer in amorphous regions [32,33,48–50]. The ground-state dimers are stably formed through π–π interactions between two neighboring phenyl rings, whereas the excimer consists of an overlapping sandwich structure of electronically excited phenyl units. According to evidence from related work by Luo et al. [32,33], we assign the fluorescence peak about 385 nm to the ground-state dimer and attribute the feature at 360 nm to fluorescence of a molecular complex formed through interaction between phenyl rings and/or among phenyl and carbonyl groups. Only the quenched amorphous film featured the fluorescence emission of the dimers because the phenyl–phenyl distance of approximately 0.55 nm in the lattice unit of PTT and isolated phenyl rings in the molten state exceed a minimum phenyl–phenyl distance 0.35 nm required for the fluorescence emission of the dimers [51].

The formation of the ground-state dimers is also confirmed from the FTIR spectrum of the band associated with CH out-of-plane bending of the phenyl rings. The FTIR spectra of various PTT films are shown in Fig. 1b. According to assignment to the CH out-of-plane bending of the phenyl rings in the crystalline phase of PTT in the literature [52,53], the band at 871 cm^{-1} appeared not only in both the crystalline states melt-crystallized at 170 °C (curve **b**) and cold-crystallized at 50 °C (curve c) but also in the molten state at 260 °C (curve a). In contrast, the FTIR spectra of various amorphous films obtained from quenched, aged and cold-drawn treatments (curves of d, e and f in Fig. 1b) display the band at 874 cm^{-1} for the CH out-of-plane bending of the phenyl rings. As the wavenumber shift of the CH out-of-plane bending mode of phenyl rings to increased wavenumber by the π–π interactions was demonstrated in varied aromatic molecules proposed by Humphrey [54], we infer that the formation of π–π stacking of phenyl rings in the amorphous films produces the 874 cm^{-1} band, whereas the band at

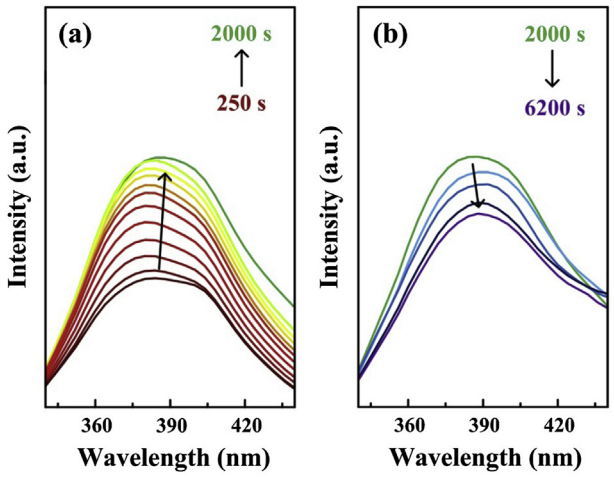

Fig. 2. Time-resolved fluorescence spectra of PTT during isothermal cold crystallization at 50 °C (λ_{ex} = 322 nm). The spectra are selectively shown before 2000 s (a) and after 2000 s (b), respectively.

871 cm^{-1} results from separated phenyl rings in the lattice unit of PTT crystals and the isolated phenyl rings in the molten states (without the π–π effect).

The band at 933 cm^{-1} was present for only the various amorphous states, including molten, quenched, aged and cold-drawn amorphous films (as shown in Fig. 1b), whereas the band at 936 cm^{-1} appeared for the crystalline films. We assign, therefore, the bands at 936 and 933 cm^{-1} to crystalline and amorphous phases for the *gauche* conformer of the inner two C–C bonds of trimethylene glycol units, respectively. From the observations of FTIR and PL data in Fig. 1, we conjecture that the PTT chains in the supercooled amorphous liquid favor forming the phenyl–phenyl dimers characterized as '*locally metastable structures*', expected to coexist with the regular amorphous phase in a kinetically trapped metastable state.

Dimer aggregation before cold crystallization. Fig. 2 shows the time evolution of fluorescent spectra during the isothermal cold crystallization of PTT at 50 °C. The fluorescent emission of the dimers shifted gradually from 385 to 390 nm with time *t*; the intensities initially increased and then decreased after ca. 2000 s. The red shift of the fluorescent signal also confirmed the presence of ground-state dimers [32]. Accordingly, Fig. 3 shows systematic changes of several characteristic bands in the time-resolved FTIR spectra observed during the cold crystallization of PTT at 50 °C. The net changes of absorbance in Fig. 3b, after subtraction of the contribution of the initial state (t = 0 s) before the isothermal crystallization, illustrate better the growth in the bands centered near 871 and 936 cm^{-1} and the decay in the bands centered about874 and 815 cm^{-1} during the cold crystallization. As shown in Fig. 3c, we observed that the band at 874 cm^{-1} appeared initially and then gradually transformed to low wavenumber (ca. 872 cm^{-1}) after approximately 2000 s during the cold crystallization.

From the results of time-resolved PL and FTIR spectra, we ascertained that both the increase in the fluorescent intensities of the dimer emission and the appearance of the band at 874 cm^{-1} for the CH out-of-plane bending mode of phenyl rings reveal an extensive aggregation of dimers and/or formation of the dimers during an induction stage of the cold crystallization, whereas the decrease of fluorescent emission and the band shift from 874 to 872 cm^{-1} arise from separating the phenyl–phenyl distance when the crystallization occurred. During the melt crystallization at 200 °C (Fig. 4), the band fixed approximately at 871 cm^{-1} rather than shifting for the CH out-of-plane bending mode of phenyl rings

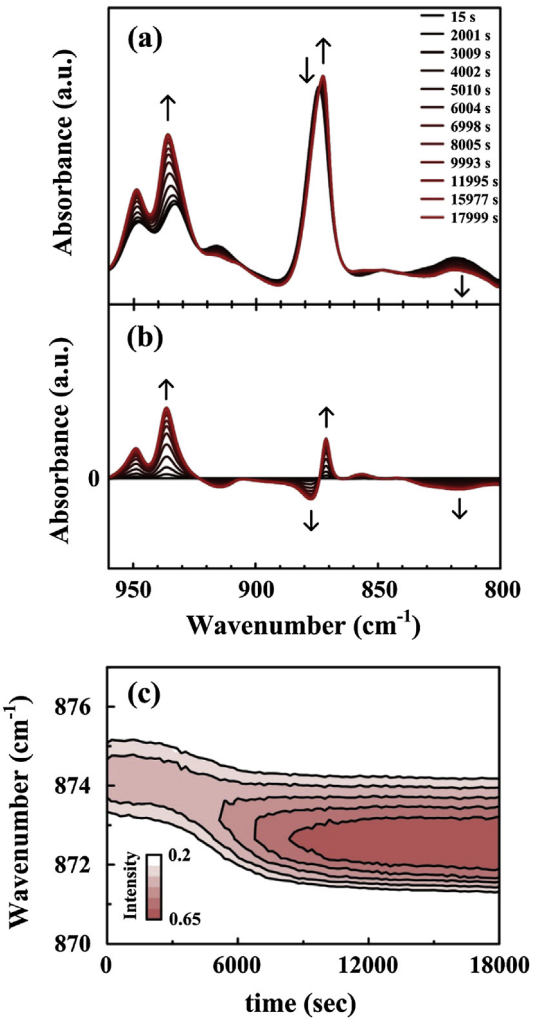

Fig. 3. (a) Time-resolved FTIR spectra of PTT measured during isothermal cold crystallization at 50 °C; (b) the difference spectra after subtraction of the first spectrum obtained at t = 0 s; (c) contour plot of the FTIR spectra in the wavenumber range 870–877 cm^{-1} for the band associated with the CH out-of-plane bending mode of the phenyl rings.

and the absence of the fluorescent emission of ground-state dimers at 390 nm (Fig. S1) indicate that the preordering chain activities of the melt crystallization at high temperatures do not undergo the dimer aggregation.

Formation of phase-separated mesomorphic domains. Shown in Figs. 5 and 6 are time-resolved WAXS and SAXS profiles during the isothermal cold crystallization of PTT at 50 °C, respectively. At an early stage of the cold crystallization (before ca. 3000 s), an unobvious shoulder at ca. q = 11 nm^{-1}, near a (010) diffraction of the PTT crystals, emerged from a broad amorphous halo centered at q = 14 nm^{-1} (Fig. 5). The foremost appearance of the (010) diffraction indicates that an ordered assembly of chains along lateral directions (normal to the chain-axis (*c*-axis) direction) precedes one along the chain-axis direction, corresponding to the direction of growth along the *b*-axis of the triclinic lattice in PTT [55]. In Fig. 6 all SAXS profiles were subtracted from the profile measured for amorphous samples with a disordered structure at t = 0 s; the original SAXS profiles without removal of the background scattering are shown in Fig. S2. According to the distinct scattering features, the SAXS profiles are characterized by division into four stages—(I) induction, (II) nucleation, (III) growth/crystallization, and (IV) ripening, consistent with the cold-crystallization

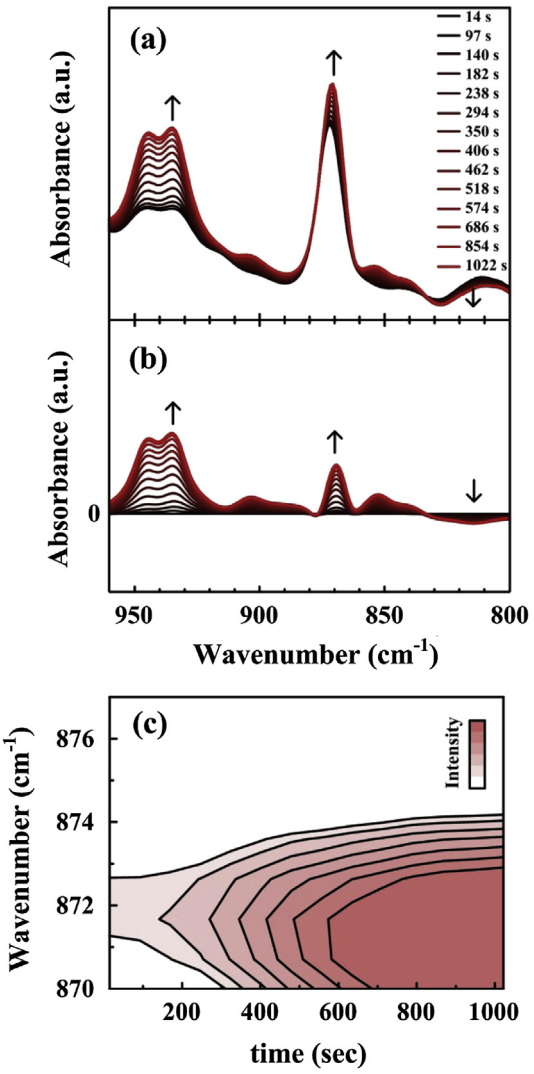

Fig. 4. (a) Time-resolved FTIR spectra of PTT measured during isothermal melt crystallization at 200 °C; (b) difference spectra after subtraction of the first spectrum obtained at $t = 0$ s; (c) contour plot of the FTIR spectra in the wavenumber range 870–877 cm^{-1} for the band associated with the CH out-of-plane bending mode of the phenyl rings.

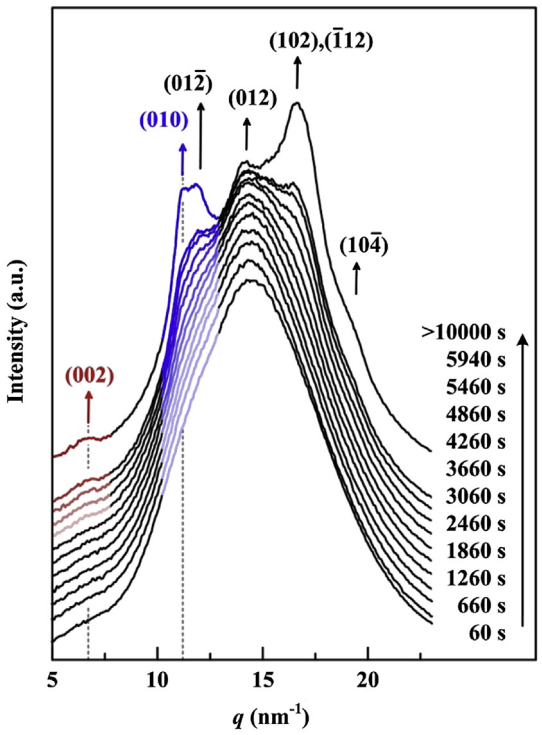

Fig. 5. Time-resolved WAXS profiles of PTT during isothermal cold crystallization at 50 °C.

behavior at 55 °C as shown previously [22]. The detailed structural characteristics are shown in the discussion section.

In contrast with the cold crystallization at 50 °C, Fig. 7a and b show time-resolved SAXS/WAXS profiles of the melt crystallization at 200 °C. The SAXS profiles displayed a typical development of a long-period peak of lamellae without the unusual small-angle scattering in the low-q range after an induction period of the melt crystallization. This result indicates that the varied preordering behavior of PTT chains features the small nanograins within the mesomorphic domains for the cold crystallization [22] but typical folding-chain lamellae within spherulites for the melt crystallization [24].

Mesostructural Dynamics. Fig. 8 shows the temporal evolution of dielectric loss curves during isothermal cold crystallization of PTT at 50 °C. These curves were collected every 60 s during 3000 s corresponding to stages I and II of the cold crystallization defined from SAXS/WAXS results. In a first spectrum at 60 s, a single α relaxation, featuring the typical segmental relaxation of amorphous chains (glassy dynamics), located about 80 Hz, beside the dc conductivity tail appearing at the smallest frequencies (Fig. 8a). Exhibiting an asymmetric breadth on the low-frequency side during the further isothermal process, the entire dielectric loss curves were decomposed into α- and α′-relaxation processes as shown in Fig. 8b and c. As the isothermal crystallization proceeded, the intensities of the α relaxation monotonically decreased but their position slightly shifted to smaller frequencies, whereas the α′ relaxation largely shifted to smaller frequencies with increased intensities and peak widths.

In the fitting procedure with the Navriliak-Hegami equation combined with a dc-conductivity term (eq (7)), the shape parameters associated with the α relaxation were fixed, and obtained from the first spectrum for a hypothetically unaltered nature of the complete amorphous phase during the crystallization to decrease the fitting parameters in eq. (7). Fig. 9a and b show the dielectric strength ($\Delta\varepsilon_\alpha$ and $\Delta\varepsilon_{\alpha'}$) and the average relaxation times τ_α and $\tau_{\alpha'}$ for the two relaxations as a function of time, respectively; other fitted parameters are shown in Fig. S3 for simplicity. The α′ relaxation arose in parallel with the dimer aggregation and formation of the mesomorphic domains in the induction stage I. From the observed results of SAXS/WAXS and fluorescence data, we conjecture that the formation of mesomorphic domains results from the dimer aggregation. Thereby, the α′ relaxation becomes identification with the mesostructural dynamics of the dimer aggregation before the cold crystallization in addition to the α relaxation characterizing the glassy dynamics.

$\Delta\varepsilon_\alpha$ decreased but $\Delta\varepsilon_{\alpha'}$ increased during the isothermal cold crystallization. This conversion from $\Delta\varepsilon_\alpha$to $\Delta\varepsilon_{\alpha'}$ indicates that the formation of the mesomorphic domains through dimer aggregation consumes the regular amorphous domains. A similar transition from α to α ′before crystallization was observed in poly(ethylene terephthalate), PET [56–58]. In Fig. 9b, the relaxation time $\tau_{\alpha'}$ featuring the chain mobility of mesomorphic domains is approximately ten times that of τ_α of the amorphous bulk phase. This result features a dynamic heterogeneity in the phase-separated domains and reflects denser chain packing in the mesomorphic domains.

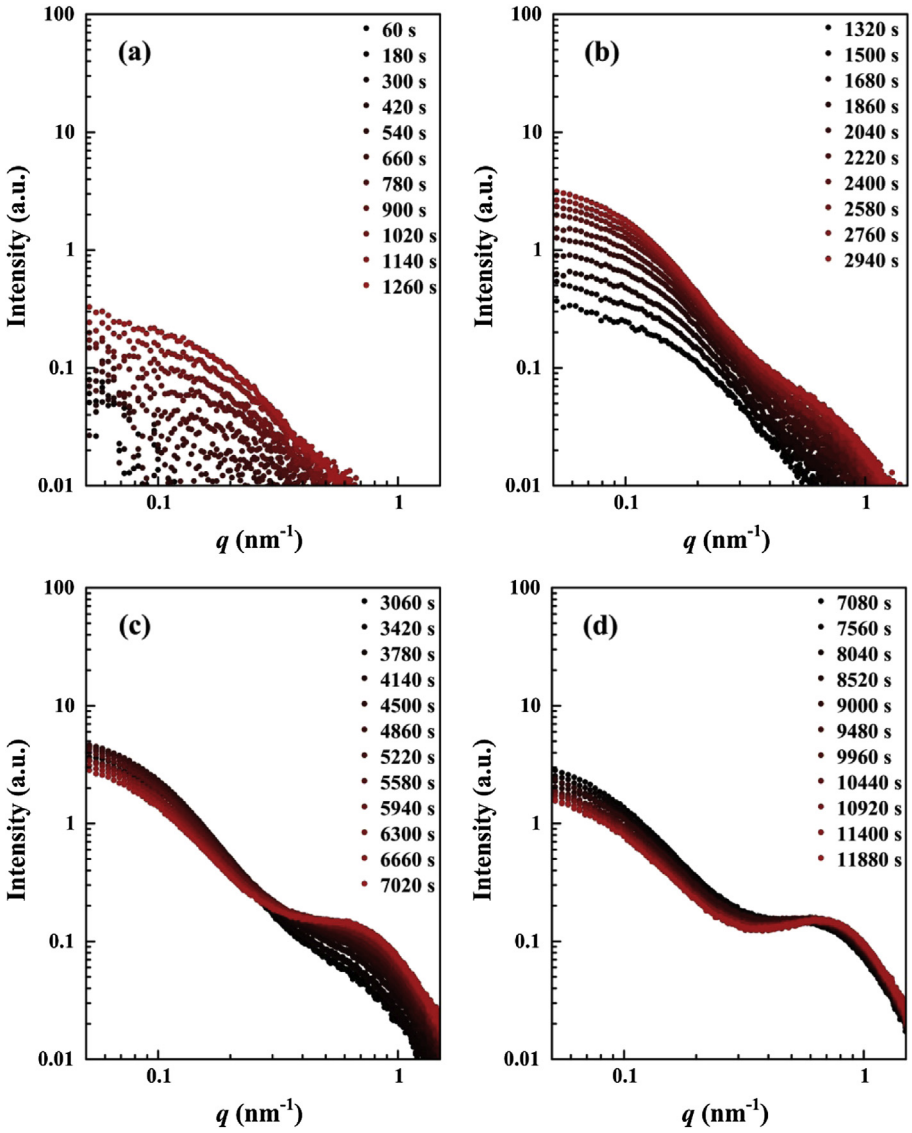

Fig. 6. Time-resolved SAXS profiles with subtraction of the first featureless profile measured at the beginning of the isothermal cold crystallization at 50 °C. The profiles are divided into four stages (a–d) according to their distinctive scattering features.

The slight increase of τ_α with increasing duration of crystallization is presumably the cause of a constraint effect by the growing mesomorphic domains.

4. Discussion

Development of Lamellar crystallites. In Fig. 10, the time dependences of the lamellar structural parameters determined from the SAXS data and the crystallinity W_c obtained from the WAXS data are compared with the intensity changes of the *trans* and *gauche* conformers revealed by FTIR data for the melt crystallization at 200 °C. In Fig. 10a, two types of the long periods are represented: one is calculated form Bragg's law, L_p ($=2\pi/q_m$, in which q_m is the peak position in the Lorentz-corrected scattering plot, i.e., Iq^2vs q), and another is calculated with the 1D correlation function, L_{1D}(= the distance in the fist maximum of $\gamma(x)$ (cf. Fig. S4)). The long period L_{1D} cannot be obtained form the weaker SAXS peak using the 1D correlation function because of a lack of lamellar correlation in an initial nucleation. The variations of the structural parameters with time can be classified into three regions across the two characteristic times about 90 and 200 s as indicated by the broken lines. In region (i), the considerable proportion of the *trans* conformers was formed from random-coil conformation in the melt. Subsequently, the conformational transformation from *trans* to *gauche* and the SAXS peak emerged in region (ii). Finally, the crystalline Bragg peak of (010) appeared after ca. 200 s, and then lamellar crystallites gradually grew in region (iii). As the transformation from *trans* to *gauche* (Fig. 10c), the SAXS peak and the increase of invariant Q were evident before the emergence of crystalline Bragg peaks in WAXS in Fig. 10b, on the basis of a typical model of crystalline lamellae we conjecture that, during the transformation from *trans* to *gauche*, the PTT segments with the *gauche* conformers, the most stable conformations, gather locally to form precursory mesomorphic layers with correlation distance ca. 12 nm obtained from L_p; the optimization of packing order resulted in the nucleation in which the cooperative segments aligned parallel form the crystalline structure stacked in lamellae constructed with long period ca. 11 nm and lamellar thickness ca. 4 nm.

Hierarchically structural evolution during cold crystallization. As distinct from the typical model of lamellar crystallites, the

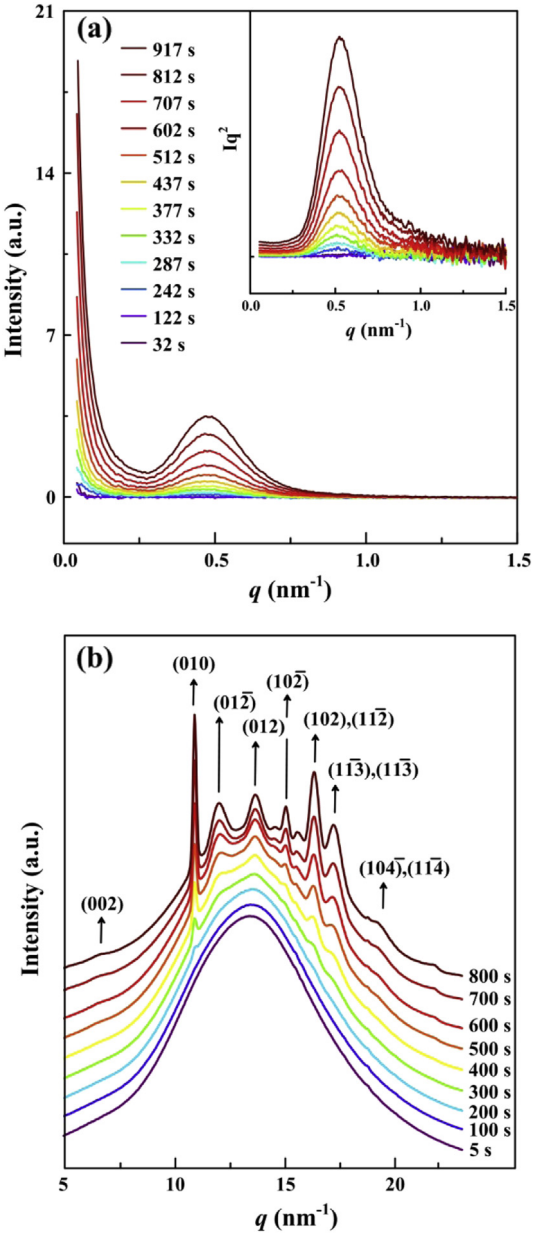

Fig. 7. Time-resolved SAXS (a) and WAXS (b) profiles during isothermal melt crystallization at 200 °C.

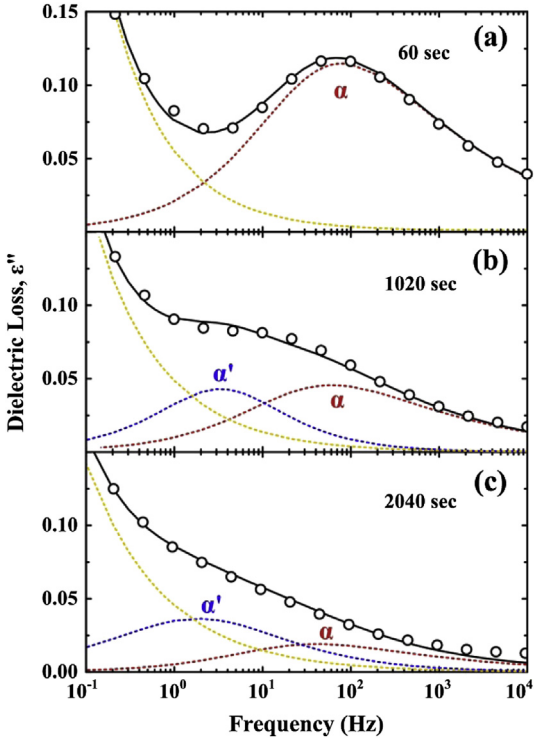

Fig. 8. Dielectric loss data as function of frequency during isothermal cold crystallization at 50 °C for 60 s (a), 1020 s (b), and 2040 s (c). The open circles represent observed values, and the solid line overlapping with the open circles was obtained with a non-linear least-squares fit to eq (7). The red and blue dotted lines denote the contributions from the α and α' relations, respectively. The yellow dotted lines are contributed from the dc conductivity. (For interpretation of the references to colour in this figure legend, the reader is referred to the web version of this article.)

morphology of cold crystallization of PTT represented the hierarchical structure of nanograins within mesomorphic domains evidenced by TEM as shown previously [22]. Thereby, we modeled, respectively, the SAXS data in the low-q region using the Guinier approximation (eq (1)) for the mesomorphic domains and in the large-q region using a disk-like disk-like form factor for the nanograins (as shown in Fig. S5); PY hard-sphere structure factor S(q) (eq (3)) was added to the fitting procedure in stage IV [22]. These fitted results are summarized in Fig. 11a. The mesomorphic domains in stage I exhibited initially a nucleation-like size D of diameter ca. 15.5 nm ($D = 2(\sqrt{5/3}R_g)$), with an assumed spherical shape. The D size gradually increased to approximately47 nm in stage III. The R_g size eventually increased too much to be detected in the limited q range. The fitted disk diameter 2$R$for the nanograins increased from 2.5 to 4.1 nm, and the thickness L increased from 1.8–2.6 nm. In the final stage, both sizes of the nanograins attained

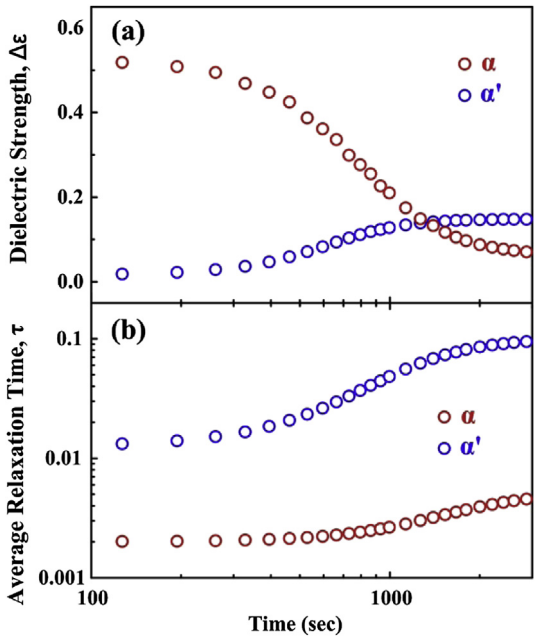

Fig. 9. Time evolution of dielectric strength (a) and average relaxation time (b) for the α and α' relaxation processes of PTT during isothermal cold crystallization at 50 °C, respectively.

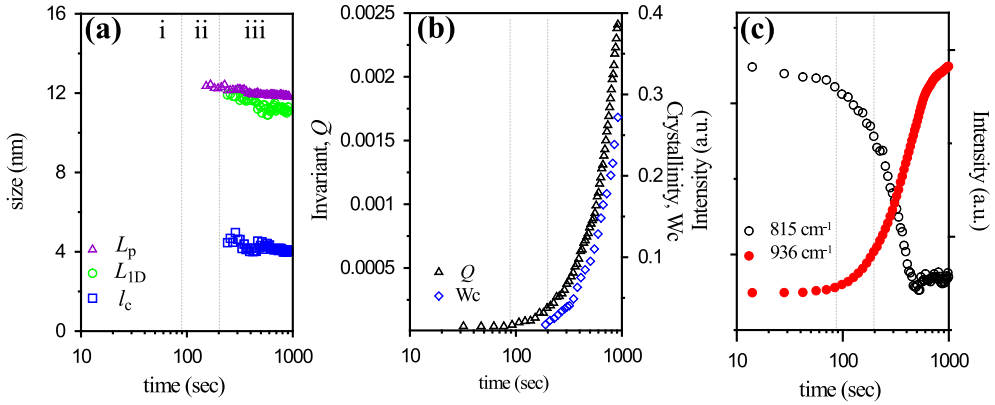

Fig. 10. Structural evolution during the melt crystallization of PTT at 200 °C: (a) lamellar thickness l_c and long periods of L_p and L_{1D} from Bragg's law and correlation function, respectively, (b) development of WAXS-defined crystallinity W_c and SAXS invariant Q, and (c) intensities of *trans* and *gauche* conformers calculated from IR bands at 815 and 936 cm^{-1}. Three assigned stages divided by gray dotted lines were described in text.

nearly plateaus, and the mean spacing of the nanograins, ξ, decreased slightly from 8 to 7.5 nm.

Based on SAXS and WAXS results we found an atypical crystallization behavior in which the structural evolution of PTT features two hierarchical levels during cold crystallization: the large-scale mesomorphic domains develop through the dimer aggregation in the induced stage I, and then the small non-crystalline nanograins, functioning as precursory embryos of nucleation, evolve within the mesomorphic domains in stage II, i.e., the formation of large mesomorphic domains (tens of nanometers) before the formation of small noncrystalline nanograins (a few nanometers). Subsequently, the crystalline nanograins grow in stage III, and the final crystallites with short-range ordering mature in stage IV.

Phase-separated mesomorphic domains induced by dimer aggregation. To understand the relation among the dimer aggregation, mesomorphic domains and nanograins during the cold crystallization, we show in Fig. 11 all time-resolved data derived from SAXS, FTIR, DS and PL, allowing us to elucidate the multistage preordering of the cold crystallization from various points of view of structural and conformational changes and chain dynamics. Before stage III (the two phases only), we estimated the fraction of amorphous domains from the ratio between the dielectric strength $\Delta\varepsilon_\alpha$ and total dielectric strength ($\Delta\varepsilon_\alpha + \Delta\varepsilon_{\alpha'}$) as well as the fraction of mesomorphic domains on the basis of the unity conservation. In Fig. 11b, the two fractions as function of time indicate that the conversion from the regular amorphous to mesomorphic domains occurred mainly in the induction stage I and then approached a plateau about 65% in stage II. Fig. 11c and d show the time dependence of the intensity of fluorescence emission of the dimers, the wavenumbers of bands associated with the CH out-of-plane bending mode of the phenyl rings and the intensities of bands at 815 and 936 cm^{-1} corresponding to the *trans* and *gauche* conformers, respectively. These results reveal that the preordering chain activity in stage I involved dimer aggregation with a large proportion of the *trans* conformers; in nucleation stage II the transformation from *trans* to *gauche* accompanied the increasing

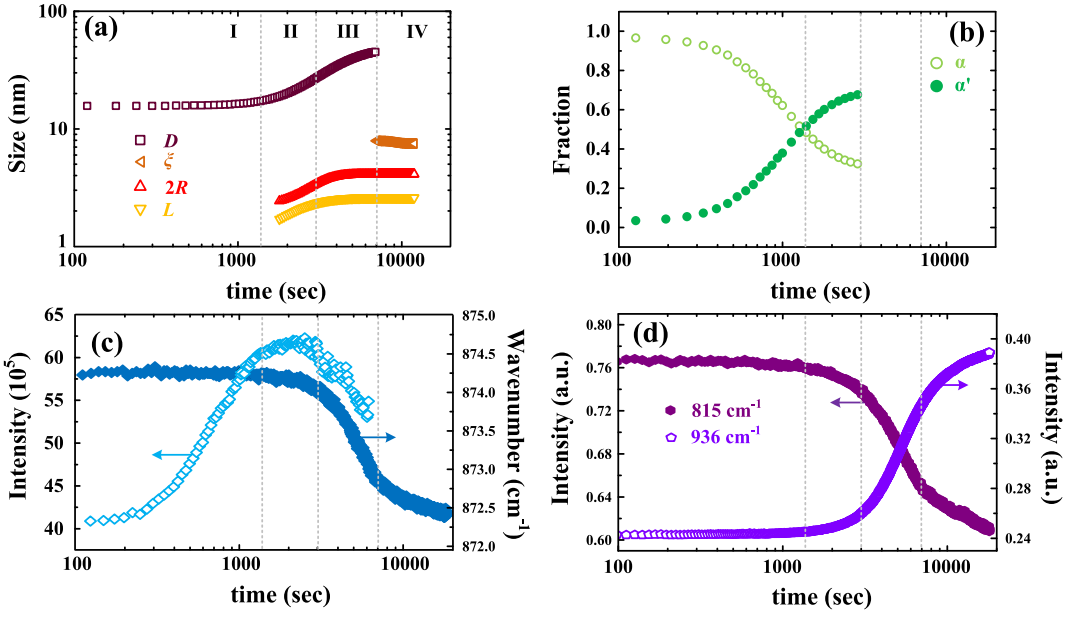

Fig. 11. Structural evolution of PTT during the isothermal cold crystallization at 50 °C: (a) diameter D of mesomorphic domain, diameter $2R$ and thickness L of disk-like nanograins and mean spacing ξ of nanograins, (b) fractions of amorphous and mesomorphic domains calculated from the dielectric strengths of $\Delta\varepsilon_\alpha$ and $\Delta\varepsilon_{\alpha'}$, (c) time-dependent intensity change of fluorescence at 385 nm, and time-dependent shift of wavenumber of an IR band at 874 cm^{-1}, and (d) intensities of *trans* and *gauche* conformers obtained from IR bands at 815 and 936 cm^{-1}. The gray dotted lines indicate the four assigned stages of (I) induction, (II) nucleation,(III) growth/crystallization, and (IV) ripening for the cold crystallization.

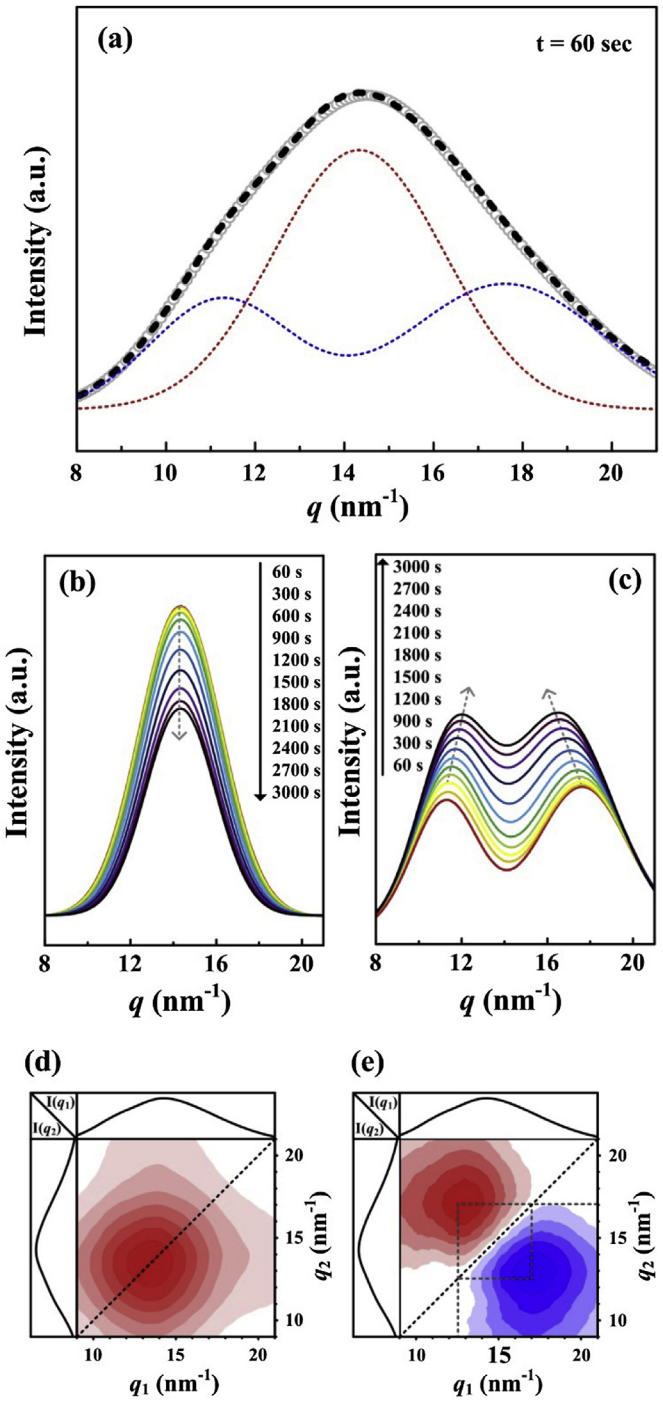

Fig. 12. (a) Selected WAXS profile (open circles) measured at t = 60 sis respectively fitted with the amorphous hump, $X_a(t)I^a(q)$, (red dotted lines) and the mesomorphic humps, $I^m(q, t)$,(blue solid lines); the time evolution of the amorphous (b) and mesomorphic(c) humps during isothermal cold crystallization at 50 °C for 0–3000 s; synchronous (d) and asynchronous (e) 2D-WAXS correlation spectra calculated from the profiles for 0–1200 s. (For interpretation of the references to colour in this figure legend, the reader is referred to the web version of this article.)

phenyl–phenyl distance, verified from the shift of wavenumber of the band from 874 to 872 cm^{-1} (Fig. 11c) and the decrease of the dimer fluorescence (Fig. 11c). These results consist with a sequential order of characteristic bands of 874 cm^{-1} > 872 cm^{-1} ≈ 933 cm^{-1} > 936 cm^{-1} obtained form the 2D-IR correlation spectra (Fig. S6).

Compared with a symmetric amorphous hump in the induction period of the melt crystallization (as shown in Fig. 7b), we observed an asymmetric amorphous hump with a small shoulder on the low-q side during cold crystallization (Fig. 5), and referred to overlapping signatures from the structural characteristics of regular amorphous and mesomorphic domains. Having obtained the two fractions of the amorphous and mesomorphic domains from the DS results (Fig. 11b), the WAXS signatures of the mesomorphic domains can hence be retrieved from $I^m(q, t) = I^{obs}(q, t) - X_a(t)I^a(q)$, in which $X_a(t)$ is the fraction of amorphous phase measured by DS, and $I^a(q)$ is a completely amorphous hump, obtained from the molten state and corrected for a thermal expansion effect. Fig. 12a demonstrates the decomposition of WAXS profiles $I^{obs}(q, t)$ at $t = 60$ s. Besides the regular amorphous hump at $q \sim 14.5$ nm^{-1}, two humps at approximately 12 and 17 nm^{-1} for the $I^m(q, t)$ signature are attributed to the mesostructural characteristics within the mesomorphic domains in induction stage I.

Fig. 12b and c show the decomposed profiles of $X_a(t)I^a(q)$ and $I^m(q, t)$ during cold crystallization before 3000 s (in stages I and II). The WAXS hump of the regular amorphous phase monotonically decreased with increasing time (Fig. 12b), whereas the intensities of the two humps in the $I^m(q, t)$ profiles increased with increasing time (Fig. 12c). Associated with the average phenyl–phenyl distance of dimers in a range ca. 0.3–0.4 nm, the $I^m(q, t)$ hump at 17 nm^{-1} shifted slightly toward the low q range after stage I (ca. 1500 s), in agreement with the increasing phenyl–phenyl distance after the transformation from *trans* to *gauche*, verified from the FTIR and PL data in Fig. 11c and d.

With the observation of a large proportion of *trans* conformers in the induction stage I (Fig. 11d), the dimers accompanying neighboring *trans* conformers along the chain axis, to a significant degree in an extended sequence, are expected to be present for rigid segments during the dimer aggregation. We hence conceive that the rigid segments attract each other via π–π interactions, and develop segments locally aligned parallel, due to minimization of the excluded volume, as a nematic-type preordering, which is similar to a concept of liquid-crystalline ordering within a mesomorphic phase reported by Kaji et al. [18]. Developing into the (010) diffraction of the triclinic lattice of PTT crystals on formation of the crystallization, the hump at ca. 12 nm^{-1} can thus be assigned to a mean distance between the nematic-like segments in the mesomorphic domains. Our finding coincides with Monte-Carlo simulations reported by Weber et al. in which the nematic-like ordering induces the unusual small-angle X-ray scattering [59].

The mesostructural characteristics were confirmed in the 2D correlation analysis proposed by Noda [44,45], which is a powerful method to treat subtle changes in spectra composed of heavily overlapped signatures and to give a sequential order among the constituent signatures [60].Fig. 12d and e show, respectively, the synchronous and asynchronous 2D correlation WAXS spectrum obtained during the cold crystallization from 0 to 1200 s (corresponding to stage I); the red and blue areas exhibit respectively the positive and negative correlation intensities. In the asynchronous 2D-WAXS spectrum, a pair of asynchronous cross peaks presented at spectral coordinates approximately 12 and 17 nm^{-1}, consistent with the two humps obtained from the decomposed WAXS profiles (Fig. 12c), but the lack of obvious correlation in the asynchronous 2D-WAXS spectrum of the melt crystallization at 200 °C (as shown in Fig. S7) supports a lack of dimer aggregation in the growth of lamellae crystallites.

Shown in Fig. 13a is a cartoon of the structural evolution of nanograins within mesomorphic domains deduced from the above discussion. Having an intrinsical heterogeneity, the quenched amorphous glass of PTT has local dimers through the π–π interactions. In stage I, the dimer aggregation forms the phase-

separated mesomorphic domains, which comprise an extended sequence of dimers with the *trans* conformers as segments aligned parallel producing a nematic-like orientation for minimization of the excluded volume. Accompanying the conformational transformation from *trans* to *gauche*, the rigid segments aligned parallel cluster into non-crystalline nanograins, which we imagine to serve as embryos of primary nucleation of PTT crystals, in stage II. This nucleation in mesomorphic domains costs a small increase of Gibbs energy upon the preordering of crystallization, but decreases greatly the surface energy, which in total leads to a greatly diminished barrier to nucleation. After fine arrangement of the segments within the nanograins, the 3D order of chain packing occurs to stabilize the nanograins. Subsequently, loosely interconnected mesomorphic domains, each filled with crystallized nanograins, continually grow in stage III; the multistage agglomerates comprised of the preordered network of mesomorphic domains filled with crystallites with short-range order are formed in the final ripening stage IV.

The structural evolution to form the lamellar structure is illustrated schematically in Fig. 13b for comparison with the cold crystallization. Our experimental results indicate that the dimer aggregation is responsible for the greatly disparate morphological features between the melt and cold crystallizations, which have different kinetic routes. The π–π interactions, which constitute a weak force but which exist to a considerable extent among the dimers, serve as ordering bonding forces to assemble neighboring segments in which the system is trapped under supercooled amorphous liquids for the cold crystallization. In the case of melt crystallization at 200 °C, the large thermal fluctuations are disadvantageous for dimer aggregation, whereas a large mobility of chains allows formation of large lamellae through chain sliding diffusion and disentanglement of chains for chain folding.

5. Conclusion

Using various time-resolved measurements of SAXS/WAXS, PL, FTIR and DS spectra, we investigated the multistage preordering activities associated with a hierarchically structural evolution of nanograins within mesomorphic domains in the PTT cold crystallization at 50 °C as well as the structural evolution of lamellar crystallites in the PTT melt crystallization at 200 °C. Integration of these time-resolved data allows us to understand a scenario of the formation of phase-separated domains before the cold crystallization. During the cold crystallization, the rigid segments, composed of dimers with *trans* conformers, accompanied with nematic-like orientation under dimer aggregation via π–π interactions, induces mesomorphic domains on a large scale; subsequently, the lateral adjustments of the segments formnanograin-type nucleations within the mesomorphic domains. As the dimers are favorably formed in quenched amorphous glass, the melt crystallization at 200 °C represents the typical crystalline lamellae without the largely phase-separated mesomorphic domains. We propose the mechanism of the cold crystallization of PTT in which the formation of mesomorphic domains through the dynamically driven dimer aggregation is related to the liquid-liquid phase separation before the cold crystallization of PTT; however, the temperature

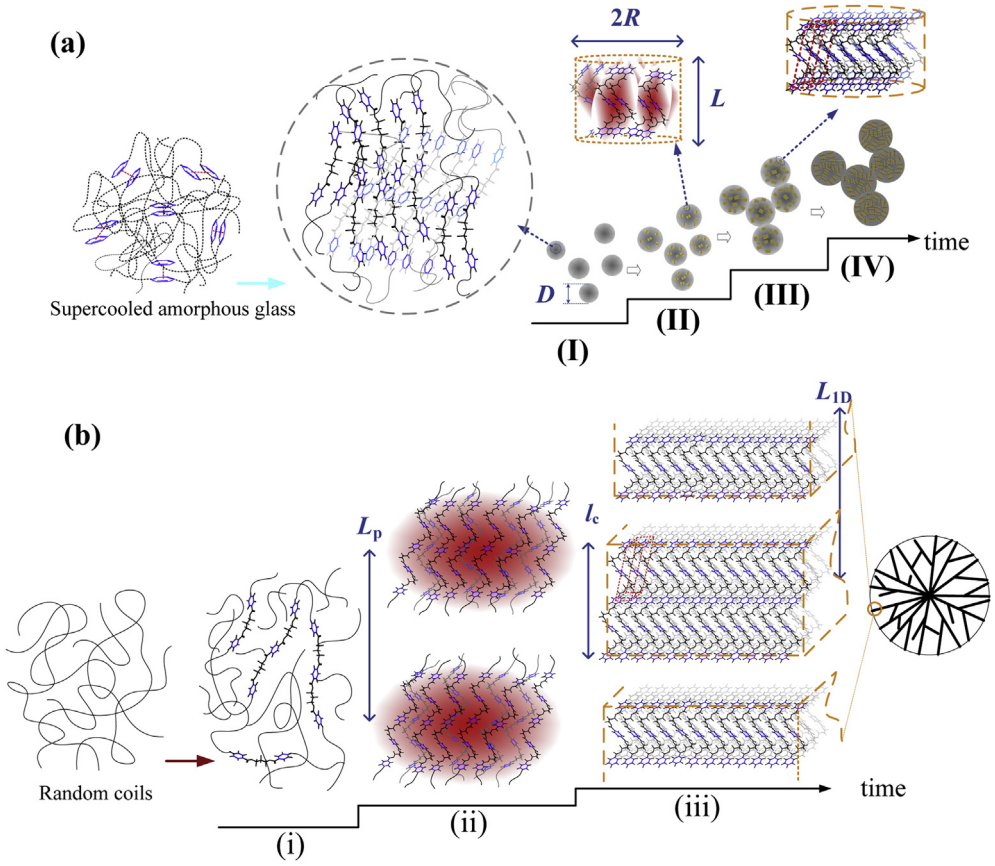

Fig. 13. Schematic illustrations of (a) the proposed evolution of an hierarchical structure during the cold crystallization of PTT at 50 °C: (I) dimer aggregations with *trans* conformers induce mesomorphic domains for the induction stage, (II) the conformational transformation from *trans* to *gauche* accompanying the formation of noncrystalline nanograins within the mesomorphic domains for the nucleation stage, (III) interconnected mesomorphic domains, each filled with crystallized nanograins for the growth stage, (IV) the percolated network of mesomorphic domains filled with nanograins during the final ripening and (b) the structural evolution of spherulites at the melt crystallization of PTT at 200 °C: (i) most disordered trans conformers in the supercooled melting state, (ii) formation of precursory mesomorphic layers, (iii) the lamellar crystallites.

dependence of this phase-separated mechanism, which remains unclear, bears investigation in a future work.

Acknowledgments

We thank Ms. K.-F. Liao and Mr. W.-B. Su for the help in SAXS measurements. Financial support from the National Science Council (Grant Numbers: NSC 99-2218-E-213-001-MY3) is gratefully acknowledged.

Appendix A. Supplementary data

Supplementary data related to this article can be found at http://dx.doi.org/10.1016/j.polymer.2013.09.006.

References

[1] Hoffman JD, Thomas DG, Lauritzen Jr JI. In: Hannay NB, editor. Treatise on solid state chemistry, vol 3. New York: Plemum Press; 1976.
[2] Wunderlich B. Macromolecular physics, vols. 1 and 2. New York: Academic Press; 1976.
[3] Strobl G. The physics of polymers. Berlin Heidelberg, New York: Springer; 1995.
[4] Allegra G, Meille SV. Adv Polym Sci 2005;191:87–135.
[5] Muthukumar M. Adv Polym Sci 2005;191:241–74.
[6] Hikosaka M, Watanabe K, Okada K, Yamazaki S. Adv Polym Sci 2005;191:137–86.
[7] Hosemann R. J Appl Phys 1963;34:25–41.
[8] Natta G. Makromol Chem 1960;35:94–131.
[9] Yeh GSY, Geil PH. J Macromol Sci Phys B 1967;1:235–49.
[10] Allerga G. J Chem Phys 1977;66:5453–63.
[11] Liu C, Muthukumar M. J Chem Phys 1998;109:2536–42.
[12] Strobl G. Eur Phys J.E 2000;3:165–83.
[13] Su CH, Jeng US, Chen SH, Lin SJ, Ou YT, Chuang WT, et al. Macromolecules 2008;41:7630–6.
[14] Su CH, Jeng US, Chen SH, Lin SJ, Wu WR, Chuang WT, et al. Macromolecules 2009;42:6656–64.
[15] Wu WR, Chuang WT, Jeng US, Su CJ, Chen SH, Chen CY, et al. Polymer 2012;53:3928–36.
[16] Imai M, Mori K, Mizukami T, Kaji K, Kanaya T. Polymer 1992;33:4451–5.
[17] Imai M, Mori K, Mizukami T, Kaji K, Kanaya T. Polymer 1992;33:4457–62.
[18] Kaji K, Nishida K, Kanaya T, Matsuba G, Konishi T, Imai M. Adv Polym Sci 2005;191:187–240.
[19] Terrill NJ, Fairclough PA, Towns-Andrews E, Komanschek BU, Young RJ, Ryan AJ. Polymer 1998;39:2381–5.
[20] Ryan AJ, Fairclough JPA, Terrill NJ, Olmsted PD, Poon WCK. Faraday Discuss 1999;112:13–29 and references cited therein.
[21] Olmsted PD, Poon WCK, McLeish TCB, Terrill NJ, Ryan AJ. Phys Rev Lett 1998;81:373–6.
[22] Chuang WT, Su WB, Jeng US, Hong PD, Su CJ, Su CH, et al. Macromolecules 2011;44:1140–8.
[23] Chuang WT, Yeh WJ, Hong PD. J Appl Polym Sci 2002;83:2426–33.
[24] Hong PD, Chuang WT, Hsu CF. Polymer 2002;43:3335–43.
[25] Hong PD, Chuang WT, Yeh WJ, Lin TL. Polymer 2002;43:6879–86.
[26] Chuang WT, Hong PD, Chuah HH. Polymer 2004;45:2413–25.
[27] Chuang WT, Hong PD, Shih KS. Polymer 2004;45:8583–92.
[28] Khan AN, Hong PD, Chuang WT, Shih KS. Mater Chem Phys 2010;119:93–9.
[29] Debye P, Bueche AM. J Appl Phys 1949;20:518–25.
[30] Fisher EW. Physica A 1993;201:183–206.
[31] Kanaya T, Patkowski A, Fisher EW, Seils J, Glaser H, Kaji K. Acta Polym 1994;45:137–42.
[32] Luo W, Liao Z, Yan J, Li Y, Chen X, Mai K, et al. Macromolecules 2008;41:7513–8.
[33] Luo W, Chen Y, Chen X, Liao Z, Mai K, Zhang M. Macromolecules 2008;41:3912–8.
[34] Jeng US, Su CH, Su CJ, Liao KF, Chuang WT, Lai YH, et al. J Appl Cryst 2010;43:110–21.
[35] Lai YH, Sun YS, Jeng US, Lin JM, Lin TL, Sheu HS, et al. J Appl Cryst 2006;39:871–7.
[36] Feigin LA, Svergun DI. Structure analysis by small-angle X-ray and neutron scattering. New York: Plenum; 1987.
[37] Percus JK, Yevick GJ. Phys Rev 1958;110:1–13.
[38] Ashcroft NW, Lekner J. Phys Rev 1966;145:83–90.
[39] Kaler EN, Bennett KE, Davis HT, Scriven LE. J Chem Phys 1983;79:5673–84.
[40] Strobl GR, Schneider M. J Polym Sci Part B: Polym Phys 1980;18:1343–59.
[41] Ruland WJ. J Appl Crystallogr 1971;4:70–3.
[42] Deby P, Bueche AM. J Appl Phys 1949;20:518–25.
[43] Deby P, Anderson Jr HR, Brumberger H. J Appl Phys 1957;28:679–83.
[44] Noda I. Appl Spectrosc 1993;47:1329–36.
[45] Noda I, Ozaki Y. Two-dimensional correlation spectroscopy. Chichester, UK: John Wiley & Sons; 2004.
[46] Havriliak S, Negami S. Polymer 1967;8:161–210.
[47] Sanz A, Nogales A, Ezquerra TA, Soccio M, Munari A, Lotti N. Macromolecules 2010;43:671–9.
[48] Sonnenschein MF, Roland CM. Polymer 1990;31:2023–6.
[49] Itagki H, Iangaki Y, Kobayashi N. Polymer 1996;37:3553–8.
[50] Hennecke M, Kurz K, Fuhrmann J. Macromolecules 1992;25:6190–4.
[51] Itagki H, Horie K, Mita I. Prog Polym Sci 1990;15:361–424.
[52] Ward IM, Wilding MA. Polymer 1977;18:327–35.
[53] Kim KJ, Bae JH, Kim YH. Polymer 2001;42:1023–33.
[54] Humphrey RE. Spectrochim Acta 1961;17:93–100.
[55] Ho RM, Ke KZ, Chen. M. Macromolecules 2000;33:7529–37.
[56] Fukao K, Miyamoto Y. Phys Rev Lett 1997;79:4613–6.
[57] Lund R, Alegría A, Goitandía L, Colmenero J, González MA, Lindner P. Macromolecules 2008;41:1364–76.
[58] Brás RA, Viciosa MT, Wang Y, Dionísio M, Mano JF. Macromolecules 2006;39:6513–20.
[59] Weber H, Paul W, Binder K. Phys Rev Lett 1997;78:2136–9.
[60] Guo L, Spegazzini N, Sato H, Hashimoto T, Masunaga H, Sasaki S, et al. Macromolecules 2012;45:313–28.